Nonlinear Control Operation of DFIG-Based WECS Incorporated With Machine Loss Reduction Scheme

Ifte Khairul Amin, *Member, IEEE*, and Mohammad Nasir Uddin, *Senior Member, IEEE*

***Abstract*—This article presents a novel adaptive backstepping based nonlinear control scheme incorporated with machine loss reduction and parameter uncertainties for grid-connected doubly fed induction generator (DFIG) driven wind energy conversion system (WECS). The proposed nonlinear controller is developed to stabilize both the grid and rotor side current control loops of direct-drive DFIG-based WECS. Traditional feedback linearization controllers are sensitive to system parameter variations and disturbances on DFIG-based WECS, which demands advanced control techniques for stable and efficient performance considering the nonlinear system dynamics. The proposed nonlinear controller incorporates the system uncertainty and nonlinearities while ensuring the stability of the drive system through Lyapunov stability criteria. A machine loss reduction algorithm is also incorporated to achieve enhanced efficiency. The performance of the proposed nonlinear scheme is compared with conventional benchmark fixed gain proportional-integral control and sliding mode control scheme for the rotor-side converter controller. The proposed nonlinear controller for DFIG-based WECS integrated with machine loss reduction scheme is successfully implemented in real time using DSP board DS 1104 for a prototype 350 W DFIG. The simulation and experimental results prove the efficacy of the proposed scheme under variable operating conditions such as wind speed variation, grid voltage disturbances, and parameter uncertainties.**

***Index Terms*—Nonlinear control, doubly fed induction generator, parameter uncertainties, loss minimization, wind energy conversion.**

NOMENCLATURE

$v_{ds}, v_{qs}, v_{dr}, v_{qr}, v_{\rm dc}, v_{qc}$	*d-q* axis stator, rotor, grid converter voltages (V).
$i_{ds}, i_{qs}, i_{dr}, i_{qr}, i_{\rm dc}, i_{qc}, i_{dfe}, i_{qfe}, i_{dm}, i_{qm}$	*d-q* axis stator, rotor, grid converter, core resistance and magnetization currents (A).
$\psi_{ds}, \psi_{qs}, \psi_{dr}, \psi_{qr}$	*d-q* axis stator and rotor flux-linkages (Wb).
R_s, R_r, R_{fe}	Stator, rotor, and core loss resistances (Ω).
ω_s, ω_r	Synchronous and rotor electrical angular speed (rad/s).
P	Number of pole pairs.
$L_s = L_{\sigma s} + L_m$	Stator self-inductance (H).
$L_r = L_{\sigma r} + L_m$	Rotor self-inductance (H).
$L_{\sigma s}, L_{\sigma r}$	Stator and rotor leakage inductances (H).
L_m	Magnetizing inductance (H).
T_e	Electromagnetic developed torque (N-m).
$\hat{x}$	Estimated value of the variable *x*.
T_t	Turbine torque (N-m).
$\dot{x}$	First derivative of the variable *x*.
$x^*, x_{\rm ref}$	Reference value or set point of the variable *x*.

Manuscript received October 16, 2018; revised January 26, 2019, May 16, 2019, and August 29, 2019; accepted November 11, 2019. Date of publication November 19, 2019; date of current version March 13, 2020. This work was supported by the Natural Science and Engineering Research Council (NSERC), Canada under the Discovery Grants-Individual program under Grant 50-14150131. Recommended for publication by Associate Editor B. G. Fernandes. *(Corresponding author: Mohammad Nasir Uddin.)*

I. K. Amin is with the Department of Electrical and Electronic Engineering, Shahjalal University of Science and Technology, Sylhet, Bangladesh (e-mail: iamin@lakeheadu.ca).

M. N. Uddin is with the Department of Electrical Engineering, Lakehead University, Thunder Bay, ON P7B 6Z6, Canada (e-mail: muddin@lakeheadu.ca).

Color versions of one or more of the figures in this article are available online at http://ieeexplore.ieee.org.

Digital Object Identifier 10.1109/TPEL.2019.2955021

I. INTRODUCTION

TO FULFILL the persistent necessity of renewable power sources, wind power has emerged as one of the most popular sustainable resources throughout the world. Doubly fed induction generators (DFIGs) have achieved a remarkable place in wind power generation industry farms because of its ability to extract maximum power at variable wind speed and decoupled active and reactive power control [1]. Various control strategies have been implemented so far by researchers for effective control of grid-connected DFIG. The conventional vector control design of DFIG-based wind power system involves cascaded control loops where simple proportional-integral (PI) controllers are executed to regulate the currents [2], [3]. A major drawback of the PI controller is that its gain tuning requires accurate knowledge of system parameters. The PI control loop may lead to instable condition due to excessive integral gain if the machine and grid filter parameters are not precisely known in DFIG-based wind energy conversion system (WECS). Hence, direct power control (DPC) and direct torque control of DFIGs have been introduced as the alternative of the conventional vector control scheme [4]–[6]. However, large power or torque ripple and variable switching frequency are the two major drawbacks of these approaches [7]. As feedback linearization method requires the precise value of the model parameters and this technique often ignores some useful nonlinearity, nonlinear control techniques have been approached as an efficient method of machine control [8]–[13].

In DFIG-driven WECS, nonlinear control is preferred because of the nonlinear coupling among generator currents and the rotor speed as well as the presence of nonlinearity in the torque equation. Since DFIG inherits nonlinear magnetization characteristics, a well-developed nonlinear control technique is necessary to achieve enhanced dynamic behavior for the control operation of the system. Adaptive backstepping based nonlinear control is considered as a suitable method for DFIG-based

WECS since the method has the ability to cope with parameter uncertainties. So far, in the wind power industry, research works have been conducted mostly on nonlinear control operation of permanent magnet synchronous generator based wind energy applications [8], [9]. However, a backstepping algorithm based power control strategy of DFIG has been presented by Xiong and Sun in [10] under normal and harmonic grid voltage to achieve better dynamic performance. A simulation study of the adaptive backstepping algorithm for maximum power point tracking (MPPT) control is outlined in [11], which includes grid-connected DFIG-WECS. Azzaoui *et al.* [12] have presented a similar approach to control electromagnetic torque and reactive power by regulating the rotor side and grid-side converter utilizing Lyapunov stability criterion. However, in these papers, adaptive backstepping based control strategies are studied only in simulation. Also, parameter adaption has not been evaluated in most of these analyses. An observer-based online parameter estimation technique for DFIG has been proposed in [13]. In [14], FPGA-based experimentation is presented. An adaptive pole placement control approach is integrated with adaptive backstepping based nonlinear control system in it. The control system utilizes Lyapunov technique to achieve MPPT along with stable output although the control of grid-side converter and regulation of dc-link voltage has not been studied in this article. Resonant-based backstepping DPC strategy is developed by Wang *et al.* [15]. The experimental results suggest better control over reactive power regulation and current total harmonic distortion (THD) under normal and harmonic grid voltage. But, the system's performance is not analyzed under variable wind speed and machine parameter variations. These studies only suggest the solutions related to the obstacles in DFIG converter control to a partial extent. Hence, a comprehensive nonlinear adaptive control technique is required to guarantee the global stability of the DFIG-WECS under grid voltage fluctuation and wind speed variation with parameter adaptation. This article presents a thorough solution for nonlinear converter control of DFIG-WECS considering the aspects mentioned earlier with detailed simulation study and hardware implementation of the design on a laboratory prototype.

There have been improvements in the machine design, utilization of advanced materials, and construction techniques. However, generator loss reduction scheme is still largely dependent on control strategies, particularly when the generators are driven by low torque. It is evident that avoidance of iron losses in DFIG model causes error in flux estimation, slip, and torque calculation. The error leads to performance deterioration especially, in low power machine where iron power loss margin is not negligible compared to the generated power. Only a handful of researchers have focused on the minimization of power loss in DFIG for wind power applications. A sliding mode control (SMC) approach is proposed in [16] to regulate the rotor current of a DFIG in order to maintain maximum power and reduce copper loss. A mathematical model is developed by Chen *et al.* in [17] to determine proper rotor current commands, which give maximum mechanical power and minimum loss based on the measured generator speed. However, all the proposed models of DFIG loss reduction are based on analytical model and tested only in the simulation platform. Practical implementation for iron loss model based loss minimization control technique for DFIG-based WECS has not been reported in any of the literature. Therefore, in this article, a nonlinear control algorithm is proposed to regulate the extracted power from wind turbine incorporating machine loss minimization technique for iron-loss based model of DFIG. The conference version of this article [18] manifests the simulation model of the nonlinear control of DFIG-WECS with stability analysis and parameter adaptation. As a subsequent extension to the work presented in [18], the first contribution of this article is the development of an adaptive backstepping based nonlinear controller incorporating core-loss resistance of DFIG to ensure precise control of the system under MPPT condition. The second attribute is the estimation of the magnetizing reactance by utilizing the parameter update laws through the adaptive backstepping technique. The performance of nonlinear controller is compared with fixed-gain PI controller and conventional sliding mode controller for RSC control. It is found that proposed controller demonstrates better performance compared to its counterparts in terms of speed and current errors reduction. The third contribution is the formulation of a machine model-based loss minimization algorithm to reduce total resistive power loss in the DFIG-based WECS. To the best of the authors' knowledge, successful real-time application of machine loss minimization based nonlinear control technique incorporating the effect of iron-loss component for DFIG driven WECS has not been reported before in other literature. This article has unified all these features in the controller design and shows effective implementation in real-time environment.

This article is organized as follows. Sections III and IV illustrate the analytical model of the proposed WECS and nonlinear controller, respectively. Section V presents the parameter adaptation rule. The development of loss reduction is presented in Section VI. Section VII shows the simulation outcomes of the proposed scheme and the real-time implementation results from the laboratory prototype model are illustrated in Section VIII to validate the simulation outcomes. Finally, the findings of the investigation have been highlighted in the conclusion section.

II. Description of the WECS

In grid-connected DFIG-based WECS, back-to-back converters are connected at the rotor side and grid side.

The converters are controlled independently by the controller-generated pulsewidth modulation (PWM) signal. A typical model of grid-connected DFIG-WECS is employed in this article where the rotor-side and grid-side converters (GSCs) are driven by the nonlinear controller. Fig. 1 illustrates the configuration of overall WECS with controller blocks [18]. An MPPT controller is incorporated in the system to maximize the generated output power. The MPPT algorithm is developed based on traditional hill-climb search (HCS) method. The HCS algorithm tracks the peak power point by utilizing the instantaneous wind speed data and evaluates the corresponding reference rotor speed for the nonlinear controller. The nonlinear controller is designed to ensure the stability of the system under variable operating condition. The dynamic model of DFIG is utilized to develop the controller equations. Table I summarizes the wind turbine and DFIG parameters for simulation and real-time experimentation.

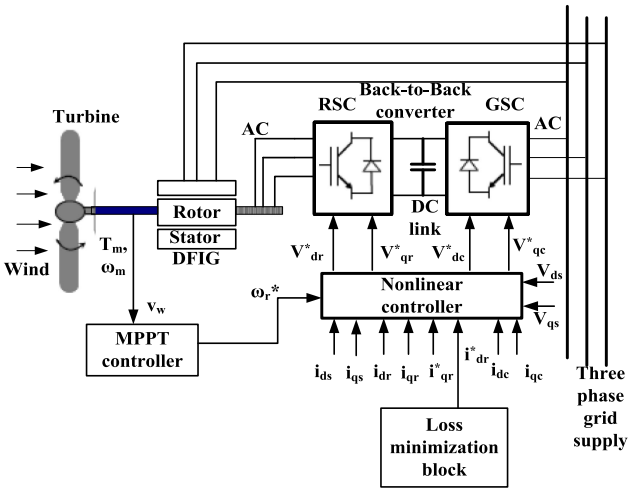

Fig. 1. Configuration of DFIG-based WECS with nonlinear controller.

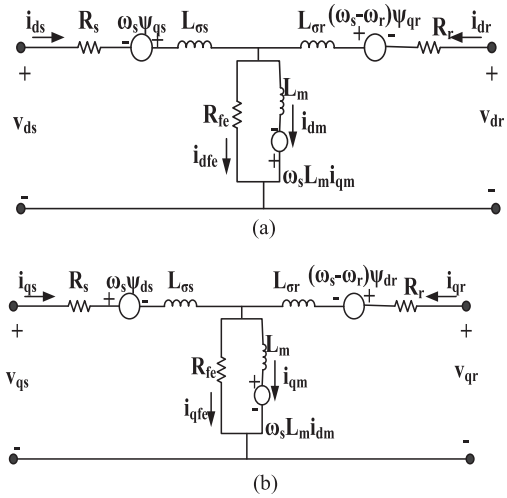

Fig. 2. (a) *d*-axis. (b) *q*-axis equivalent circuit of DFIG in synchronous reference frame referred to stator side.

TABLE I
WIND TURBINE, DFIG, AND LOAD PARAMETERS

Parameters	Simulation data	Real-time Machine data
Rated turbine power	2 MW	450 W
Blade radius	42 m	0.2 m
Rated generator power	2 MW	350 W
Grid voltage(rms)	690 V	120 V
Grid frequency	60 Hz	60 Hz
Number of pole pairs	2	2
Winding resistance	0.187 Ω	8.1 Ω
Leakage inductance	0.003 H	0.03 H
Magnetizing inductance	2.5 mH	0.477 H
dc bus capacitance	200 mF	4.2 mF
Rated dc bus voltage	1150 V	308 V
Nominal core loss resistance	66 kΩ	22 kΩ

III. ANALYTIC MODEL OF DFIG AND NONLINEAR CONTROLLER

The differential equations representing the model of DFIG can be derived from the ideal three-phase, three windings (stator and rotor) configuration of ac induction machine. The equations representing the dynamic model of DFIG are displayed in (1)–(15) obtained from the state-space model in synchronous rotating reference frame. The d-q transformation of three-phase ac quantities eliminates the effect of time-varying inductances [19].

Fig. 2 represents the d-q equivalent circuit model of DFIG in synchronous coordinate [20]. It is assumed that all the magnitudes and parameters of the rotor are referred to the stator side

$$v_{ds} = R_s i_{ds} + p\psi_{ds} - \omega_s \psi_{qs} \tag{1}$$

$$v_{qs} = R_r i_{dr} + p\psi_{qs} + \omega_s \psi_{ds} \tag{2}$$

$$v_{dr} = R_r i_{dr} + p\psi_{dr} - (\omega_s - \omega_r)\,\psi_{qr} \tag{3}$$

$$v_{qr} = R_r i_{qr} + p\psi_{qr} + (\omega_s - \omega_r)\,\psi_{dr} \tag{4}$$

$$\psi_{ds} = L_{\sigma s} i_{ds} + L_m i_{dm} \tag{5}$$

$$\psi_{qs} = L_{\sigma s} i_{qs} + L_m i_{qm} \tag{6}$$

$$\psi_{dr} = L_{\sigma r} i_{dr} + L_m i_{dm} \tag{7}$$

$$\psi_{qr} = L_{\sigma r} i_{qr} + L_m i_{qm} \tag{8}$$

$$i_{dm} = i_{ds} + i_{dr} - i_{dfe} \tag{9}$$

$$i_{qm} = i_{qs} + i_{qr} - i_{qfe} \tag{10}$$

$$L_m \frac{di_{dm}}{dt} = R_{fe} i_{dfe} + \omega_s L_m i_{qm} \tag{11}$$

$$L_m \frac{di_{qm}}{dt} = R_{fe} i_{qfe} - \omega_s L_m i_{dm} \tag{12}$$

$$\frac{J}{P}\frac{d\omega_r}{dt} = T_e - T_t \tag{13}$$

$$T_e = \frac{3PL_m}{2}(i_{dm} i_{qr} - i_{qm} i_{dr}) \tag{14}$$

$$\dot{\omega}_r = \frac{P}{J}(T_e - T_t) = \frac{P}{J}\left\{\frac{3PL_m}{2}\left(i_{dm} i_{qr} - i_{qm} i_{dr}\right) - T_t\right\}. \tag{15}$$

The symbols are defined in the nomenclature section. The stator voltage (v_s), the rotor voltage (v_r), the stator flux (ψ_s), the rotor flux (ψ_r) , and the equations of DFIG have been decomposed to *d-q* axis equations in (1)–(8) by performing abc-*dq* conversion. The derivation of the voltage, flux, and current equations can be found in [21]. The combination of the stator and rotor current is divided into core loss resistance and magnetizing inductance branches. The *d-q* axis current components through the core branches are defined in (9)–(12). The mechanical dynamics of the DFIG is expressed in (13)–(15). To maintain the stability of the DFIG system, adaptive backstepping based nonlinear feedback control method is implemented in this article. The complex nonlinear control problem is decomposed into simpler and smaller ones. In each step of the controller design, an appropriate function is derived recursively, which is

known as virtual control. At the final stage, the true control for the actual system is obtained by utilizing the Lyapunov function associated with each step. One of the important features of the backstepping design method is that parameter update laws can be obtained simultaneously with the derivation steps of control laws. Therefore, the problem associated with parameter uncertainty can be eliminated easily. The controller design starts with the machine motion equation to stabilize the actual rotor speed at the reference rotor speed. The subsystem equations are exploited and new controllers are derived by defining appropriate Lyapunov function progressively. The process terminates when the control equations for the reference voltages are derived. The state-space model of DFIG is obtained by modifying (1)–(15) while *d-q* axis stator, rotor, and core-loss current components are chosen as state variables. The state-space model equations are given as follows:

$$\frac{di_{ds}}{dt} = \frac{1}{L_{\sigma s}}\left(V_{ds} - R_s i_{ds} + \omega_s L_{\sigma s} i_{qs} - R_{fe} i_{dfe}\right) \tag{16}$$

$$\frac{di_{qs}}{dt} = \frac{1}{L_{\sigma s}}\left(V_{qs} - R_s i_{qs} - \omega_s L_{\sigma s} i_{ds} - R_{fe} i_{qfe}\right) \tag{17}$$

$$\frac{di_{dr}}{dt} = \frac{1}{L_{\sigma r}}\left(V_{dr} - R_r i_{dr} - \omega_r L_m i_{qs} + \left(\omega_s L_{\sigma r} - \omega_r L_r\right) i_{qr} - R_{fe} i_{dfe} + \omega_r L_m i_{qfe}\right) \tag{18}$$

$$\frac{di_{qr}}{dt} = \frac{1}{L_{\sigma r}}\left(V_{qr} - R_r i_{qr} + \omega_r L_m i_{ds} - \left(\omega_s L_{\sigma r} - \omega_r L_r\right) i_{dr} - R_{fe} i_{qfe} - \omega_r L_m i_{dfe}\right) \tag{19}$$

$$\frac{di_{dfe}}{dt} = \frac{V_{ds}}{L_{\sigma s}} + \frac{V_{dr}}{L_{\sigma r}} - \frac{R_s i_{ds}}{L_{\sigma s}} - \frac{\omega_r L_m i_{qs}}{L_{\sigma r}} - \frac{R_r i_{dr}}{L_{\sigma r}} - \frac{\omega_r L_r i_{qr}}{L_{\sigma r}} - \left(\frac{R_{fe}}{L_{\sigma s}} + \frac{R_{fe}}{L_{\sigma r}} + \frac{R_{fe}}{L_m}\right) i_{dfe} + \left(\frac{\omega_r L_m}{L_{\sigma r}} + \omega_s\right) i_{qfe} \tag{20}$$

$$\frac{di_{qfe}}{dt} = \frac{V_{qs}}{L_{\sigma s}} + \frac{V_{qr}}{L_{\sigma r}} - \frac{R_s i_{qs}}{L_{\sigma s}} + \frac{\omega_r L_m i_{ds}}{L_{\sigma r}} - \frac{R_r i_{qr}}{L_{\sigma r}} + \frac{\omega_r L_r i_{dr}}{L_{\sigma r}} - \left(\frac{R_{fe}}{L_{\sigma s}} + \frac{R_{fe}}{L_{\sigma r}} + \frac{R_{fe}}{L_m}\right) i_{qfe} - \left(\frac{\omega_r L_m}{L_{\sigma r}} + \omega_s\right) i_{dfe}. \tag{21}$$

A. Grid-Side Converter Control

The main purpose of the grid-side controller is to keep the dc-link voltage constant irrespective of the value and direction of the rotor power flow and to regulate the reactive power on the grid side. The GSC is assumed as a controlled voltage source that is connected to the grid with series grid-side resistance (R_g) and inductance (L_g). We assume that the state variables of the GSC controller are defined as

$x = [V_{\text{bus}}\ i_{cd}\ i_{cq}]$

where V_{bus} is the dc-link voltage, i_{cd} and i_{cq} are *d*-axis and *q*-axis grid converter currents, respectively.

The control inputs of the GSC controller are given by

$$u = [\ V_{\text{dc}}\ V_{qc}\ ]$$

where V_{dc} and V_{qc} are the *d*-axis and *q*-axis grid converter control voltages, respectively.

The dc-bus voltage (V_{bus}) is expressed in as follows:

$$CV_{\text{bus}}\frac{dV_{\text{bus}}}{dt} = P_r - P_c \tag{22}$$

where P_r and P_c are real power exchanged from the rotor-side and grid-side converters.

The error dynamics for bus voltage can be defined as

$$e_{v\text{bus}} = V_{\text{bus,ref}} - V_{\text{bus}} \tag{23}$$

$$\dot{e}_{v\text{bus}} = \dot{V}_{\text{bus,ref}} - \dot{V}_{\text{bus}} = \dot{V}_{\text{bus,ref}} - \frac{1}{CV_{\text{bus}}}(P_r - P_c). \tag{24}$$

The tracking errors of *d-q* axis GSC current components are given by (25) and (26) as follows:

$$e_{icd} = i^*_{cd} - i_{cd} \tag{25}$$

$$e_{icq} = i^*_{cq} - i_{cq} \tag{26}$$

where i^*_{cd} and i^*_{cq} are the reference grid converter currents.

The error dynamics for GSC control is obtained as follows:

$$e = [e_{v\text{bus}}\ e_{icd}\ e_{icq}]\,.$$

The objective of the GSC control is to ensure the convergence of the state variables to their corresponding reference values so that the error functions are stabilized to the equilibrium point, $e = 0$. At first, the Lyapunov function for bus-voltage error is chosen as

$$W_{e,v\text{bus}} = \frac{1}{2}e^2_{v\text{bus}}. \tag{27}$$

The derivative of (27) provides

$$\dot{W}_{e,v\text{bus}} = e_{v\text{bus}}\dot{e}_{v\text{bus}} = e_{v\text{bus}}\left\{\dot{V}_{\text{bus,ref}} - \frac{1}{CV_{\text{bus}}}\left(P_r - P_c\right)\right\}. \tag{28}$$

To nullify the dc-link voltage error, it can be assumed that

$$-k_{e,\text{bus}}e_{v\text{bus}} = \dot{V}_{\text{bus,ref}} - \frac{1}{CV_{\text{bus}}}\left(P_r - P_c\right) \tag{29}$$

$$V_{\text{bus,ref}} = \int_0^{\tau}\left\{\frac{1}{CV_{\text{bus}}}\left(P_r - P_c\right) - k_{e,\text{bus}}e_{v\text{bus}}\right\}dt. \tag{30}$$

where τ is the time when the dc-link voltage reaches the value of $V_{\text{bus,ref}}$ and $k_{e,\text{bus}}$ is a positive constant. Hence, (28) is converted into $\dot{W}_{e,\text{bus}} = -k_{e,\text{bus}}e^2_{v\text{bus}}$, which is a negative definite function.

The grid converter current dynamics are expressed in (31) and (32) by investigating the connection between the grid and GSC as follows:

$$\dot{i}_{cd} = \frac{1}{L_g}\left(V_{\text{dc}} - R_g i_{\text{dc}} + \omega_s L_{\sigma s} i_{qc} - V_{dg}\right) \tag{31}$$

$$\dot{i}_{cq} = \frac{1}{L_g}\left(V_{qc} - R_g i_{qc} - \omega_s L_{\sigma s} i_{\text{dc}} - V_{qg}\right). \tag{32}$$

The current error dynamics for the converter can be defined by utilizing (33) and (34) as

$$\dot{e}_{icd} = \dot{i}^*_{cd} - \dot{i}_{cd} = -\frac{1}{L_g}\left(V_{\rm dc} - R_g i_{\rm dc} + \omega_s L_{\sigma s} i_{qc} - V_{dg}\right) \tag{33}$$

$$\dot{e}_{icq} = \dot{i}^*_{cq} - \dot{i}_{cq} = -\frac{1}{L_g}\left(V_{qc} - R_g i_{qc} - \omega_s L_{\sigma s} i_{\rm dc} - V_{qg}\right) \tag{34}$$

where $\dot{i}^*_{cd} = \dot{i}^*_{cq} = 0$, with assumptions that the reference grid converter currents remain constant. The final Lyapunov candidate function for GSC is chosen as

$$V_1\left(e_{v\rm bus},\ e_{icd}, e_{icq}\right) = \frac{1}{2}e^2_{v\rm bus} + \frac{1}{2}e^2_{icd} + \frac{1}{2}e^2_{icq} \tag{35}$$

such that V_1 is a positive definite function, i.e., $V_1(0,0,0) = 0, V_1(e_{v\rm bus}, e_{icd}, e_{icq}) > 0$, for all $e_{v\rm bus}, e_{icd}, e_{icq} \in D - \{0\}$, where D is an open and connected subset of $\mathbb{R}^3$.

The derivative of V_1 in terms of error dynamics can be expressed as

$$\begin{aligned}\dot{V}_1 &= e_{v\rm bus}\dot{e}_{v\rm bus} + e_{icd}\dot{e}_{icd} + e_{icq}\dot{e}_{icq} \\ &= -k_{e,\rm bus}e^2_{v\rm bus} + e_{icd}\left\{-\frac{1}{L_g}\left(V_{\rm dc} - R_g i_{\rm dc} + \omega_s L_{\sigma s} i_{qc} - V_{dg}\right)\right\} \\ &\quad + e_{icq}\left\{-\frac{1}{L_g}\left(V_{qc} - R_g i_{qc} - \omega_s L_{\sigma s} i_{\rm dc} - V_{qg}\right)\right\}.\end{aligned} \tag{36}$$

The control voltages are chosen as

$$V^*_{\rm dc} = k_1 e_{icd} L_g + R_g i_{\rm dc} - \omega_s L_{\sigma s} i_{qc} + V_{dg} \tag{37}$$

$$V^*_{qc} = k_2 e_{icq} L_g + R_g i_{qc} + \omega_s L_{\sigma s} i_{\rm dc} + V_{qg}. \tag{38}$$

It is assumed that k_1 and k_2 are positive constants. After replacing the terms $V_{\rm dc}$ and V_{qc} in (36) by utilizing the corresponding voltage control from (37) and (38), the derivative of the Lyapunov candidate function becomes

$$\dot{V}_1 = -k_{e,\rm bus}e^2_{v\rm bus} - k_1 e^2_{icd} - k_2 e^2_{icq}. \tag{39}$$

With the choice of $k_{e,\rm bus}, k_1, k_2 > 0$, the function, $\dot{V}_1(e_{v\rm bus}, e_{icd}, e_{icq}) < 0$ on the domain $D = \mathbb{R}^3 - \{0\}$, i.e., is a negative definite function. Therefore, the equilibrium point, $e_{v\rm bus} = 0, e_{icd} = 0$, $e_{icq} = 0$ is globally asymptotically stable, which ensures the dc bus voltage and reference current tracking requirements are met.

B. RSC Control

The DFIG provides the feasibility of controlling the generated power for both of the super-synchronous and subsynchronous operation modes. The rotor-side converter (RSC) regulates the slip speed and controls the air-gap power of the induction machine. During the derivation of the RSC controller for adaptive backstepping based nonlinear control, it is assumed that the grid voltage remains constant. As a result, the stator current remains unchanged in balanced condition for stator voltage oriented control scheme. Therefore, the *d-q* axis stator current components (i_{ds}, i_{qs}) are considered as constants and this assumption will not affect the grid converter control because the rotor and grid converter works independently. It is also assumed that the voltage across the magnetization branch of the DFIG and the core-loss resistance are fixed at rated grid-voltage supply. Hence, the core-loss current components (i_{dfe}, i_{qfe}) are also considered as constants in the RSC controller design.

The adaptive backstepping controller design starts with the state equation for speed error function as follows:

$$\begin{aligned}\dot{e}_\omega &= \frac{P}{J}\left\{\frac{3PL_m}{2}\left(-i_{dm}i_{qr} + i_{qm}i_{dr}\right) + T_t\right\} \\ &= \frac{3P^2L_m}{2J}\left\{\left(i_{qs} - i_{qfe}\right)i_{dr} - \left(i_{ds} - i_{dfe}\right)\ i_{qr}\right\} + \frac{PT_t}{J}.\end{aligned} \tag{40}$$

In the first stage, the error function for the adapted value of the magnetization inductance is expressed as

$$e_{L1} = L_m - \hat{L}_{m1}. \tag{41}$$

The actual and first estimation for the magnetizing inductances are given as L_m and $\hat{L}_{m1}$, respectively. The Lyapunov candidate function for stabilization of rotor speed is chosen as

$$V_\omega = \frac{1}{2}e^2_\omega + \frac{1}{2}e^2_{L1} \tag{42}$$

$$\begin{aligned}\dot{V}_\omega &= e_\omega\dot{e}_\omega + e_{L1}\dot{e}_{L1} \\ &= e_\omega\left\{\frac{3P^2L_m}{2J}\left\{\left(i_{qs} - i_{qfe}\right)i_{dr} - \left(i_{ds} - i_{dfe}\right)\ i_{qr}\right\} + \frac{PT_t}{J}\right\} \\ &\quad + e_{L1}\left(-\dot{\hat{L}}_{m1}\right) \\ &= e_\omega\left\{\frac{3P^2\left(e_{L1} + \hat{L}_{m1}\right)}{2J}\left\{\left(i_{qs} - i_{qfe}\right)i_{dr}\right.\right. \\ &\qquad \left.\left. - \left(i_{ds} - i_{dfe}\right)\ i_{qr}\right\} + \frac{PT_t}{J}\right\} + e_{L1}\left(-\dot{\hat{L}}_{m1}\right) \\ &= e_\omega\left\{\frac{3P^2\hat{L}_{m1}}{2J}\left\{\left(i_{qs} - i_{qfe}\right)i_{dr} - \left(i_{ds} - i_{dfe}\right)\ i_{qr}\right\} + \frac{PT_t}{J}\right\} \\ &\quad + e_{L1}\left[\frac{3P^2e_\omega}{2J}\left\{\left(i_{qs} - i_{qfe}\right)i_{dr} - \left(i_{ds} - i_{dfe}\right)\ i_{qr}\right\} - \dot{\hat{L}}_{m1}\right] \\ &= e_\omega\left\{\frac{3P^2\hat{L}_{m1}}{2J}\left\{\left(i_{qs} - i_{qfe}\right)\left(\ i^*_{dr} - e_{idr}\right) - \left(i_{ds} - i_{dfe}\right)\right.\right. \\ &\qquad \left.\left. \times\ \left(\ i^*_{qr} - e_{iqr}\right)\right\} + \frac{PT_t}{J}\frac{3P^2\hat{L}_{m1}}{2J}\right\} \\ &\quad + e_{L1}\left[\frac{3P^2e_\omega}{2J}\left\{\left(i_{qs} - i_{qfe}\right)i_{dr} - \left(i_{ds} - i_{dfe}\right)\ i_{qr}\right\} - \dot{\hat{L}}_{m1}\right].\end{aligned} \tag{43}$$

We assume, $-k_\omega e_\omega = \frac{3P^2\hat{L}_{m1}}{2J}\{(i_{qs}-i_{qfe})i^*_{dr}-(i_{ds}-i_{dfe})i^*_{qr}\}+\frac{PT_t}{J}$

$$\dot{\hat{L}}_{m1} = \frac{3P^2 e_\omega}{2J}\left\{\left(i_{qs}-i_{qfe}\right)i_{dr}-\left(i_{ds}-i_{dfe}\right)i_{qr}\right\}$$

$$e_{idr} = i^*_{dr} - i_{dr}$$

$$\dot{e}_{idr} = \dot{i}^*_{dr} - \dot{i}_{dr}$$

$$= \dot{i}^*_{dr} - \frac{1}{L_{\sigma r}}\{V_{dr} - R_r i_{dr} - \omega_r L_m i_{qs} + (\omega_s L_{\sigma r} - \omega_r L_r) i_{qr} - R_{fe} i_{dfe} + \omega_r L_m i_{qfe}\}$$

$$e_{iqr} = i^*_{qr} - i_{qr}$$

$$\dot{e}_{iqr} = \dot{i}^*_{qr} - \dot{i}_{qr} = \dot{i}^*_{qr} - \frac{1}{L_{\sigma r}}\{V_{qr} - R_r i_{qr} + \omega_r L_m i_{ds} - (\omega_s L_{\sigma r} - \omega_r L_r) i_{dr} - R_{fe} i_{qfe} - \omega_r L_m i_{dfe}\}.$$

With these assumptions, (43) becomes

$$\dot{V}_\omega = e_\omega \dot{e}_\omega + e_{L1}\dot{e}_{L1}$$

$$= -k_\omega e_\omega^2 + \frac{3P^2\hat{L}_{m1}\left(i_{ds}-i_{dfe}\right)e_\omega e_{iqr}}{2J} - \frac{3P^2\hat{L}_{m1}\left(i_{qs}-i_{qfe}\right)e_\omega e_{idr}}{2J}. \tag{44}$$

The derivative of the Lyapunov function in (44) is a negative semidefinite function. The reference current i^*_{qr} is obtained from the assumption as follows:

$$i^*_{qr} = \frac{1}{(i_{ds}-i_{dfe})}\left\{\left(i_{qs}-i_{qfe}\right)i^*_{dr} + \frac{2T_t}{3P\hat{L}_{m1}J} + \frac{2k_\omega e_\omega}{3P^2\hat{L}_{m1}}\right\}. \tag{45}$$

Taking the derivative of i^*_{qr}, we get

$$\dot{i}^*_{qr} = \frac{1}{(i_{ds}-i_{dfe})}\left\{\left(i_{qs}-i_{qfe}\right)\dot{i}^*_{dr} - \frac{2T_t\dot{\hat{L}}_{m1}}{3P\hat{L}^2_{m1}J} + \frac{2k_\omega \dot{e}_\omega}{3P^2\hat{L}_{m1}} - \frac{2k_\omega e_\omega \dot{\hat{L}}_{m1}}{3P^2\hat{L}^2_{m1}}\right\}$$

$$= \frac{1}{(i_{ds}-i_{dfe})}\left\{-\frac{PT_t e_\omega}{\hat{L}^2_{m1}J^2}\left\{\left(i_{qs}-i_{qfe}\right)i_{dr}-\left(i_{ds}-i_{dfe}\right)i_{qr}\right\} - \frac{2{k_\omega}^2 e_\omega}{3P^2\hat{L}_{m1}} - \frac{k_\omega {e_\omega}^2}{J\hat{L}^2_{m1}}\left\{\left(i_{qs}-i_{qfe}\right)i_{dr}-\left(i_{ds}-i_{dfe}\right)i_{qr}\right\}\right\}.$$

In the second stage, the error for magnetization inductance is defined as

$$e_{L2} = L_m - \hat{L}_{m2}$$

where $\hat{L}_{m2}$ is the second estimated value for the magnetizing inductance. Next, the final Lyapunov function V_{Fp} is defined as follows:

$$V_{Fp} = V_\omega + \frac{1}{2}e^2_{idr} + \frac{1}{2}e^2_{iqr} + \frac{1}{2\beta}e^2_{L2}. \tag{46}$$

It is assumed that i^*_{dr} remains unchanged during operation and β is a positive constant with the assumptions

$$-k_3 e_{idr} = -\frac{1}{L_{\sigma r}}\Big\{V_{dr} - R_r i_{dr} - \omega_r \hat{L}_{m2} i_{qs} + (\omega_s L_{\sigma r} - \omega_r L_r) i_{qr} - R_{fe} i_{dfe} + \omega_r \hat{L}_{m2} i_{qfe}\Big\} - \frac{3P^2\hat{L}_{m1}\left(i_{qs}-i_{qfe}\right)e_\omega}{2J} \tag{48}$$

$$-k_4 e_{iqr} = \frac{1}{(i_{ds}-i_{dfe})}\left\{-\frac{PT_t e_\omega}{\hat{L}^2_{m1}J^2}\left\{\left(i_{qs}-i_{qfe}\right)i_{dr} - \left(i_{ds}-i_{dfe}\right)i_{qr}\right\} - \frac{2{k_\omega}^2 e_\omega}{3P^2\hat{L}_{m1}} - \frac{k_\omega {e_\omega}^2}{J\hat{L}^2_{m1}} \times \left\{\left(i_{qs}-i_{qfe}\right)i_{dr} - \left(i_{ds}-i_{dfe}\right)i_{qr}\right\}\right\} - \frac{1}{L_{\sigma r}}\Big\{V_{qr} - R_r i_{qr} + \omega_r \hat{L}_{m2} i_{ds} - (\omega_s L_{\sigma r} - \omega_r L_r) i_{dr} - R_{fe} i_{qfe} - \omega_r \hat{L}_{m2} i_{dfe}\Big\} + \frac{3P^2\hat{L}_{m1}\left(i_{ds}-i_{dfe}\right)e_\omega}{2J} \tag{49}$$

$$\frac{1}{L_{\sigma r}}e_{idr}\omega_r i_{qs} - \frac{1}{L_{\sigma r}}e_{idr}\omega_r i_{qfe} - \frac{1}{L_{\sigma r}}e_{iqr}\omega_r i_{ds} + \frac{1}{L_{\sigma r}}e_{iqr}\omega_r i_{dfe} - \frac{\dot{\hat{L}}_{m2}}{\beta} = 0 \tag{50}$$

where k_3 and k_4 are positive constants.

We obtain control laws by utilizing (48) and (49) as

$$V^*_{dr} = k_3 e_{idr} L_{\sigma r} + R_r i_{dr} + \omega_r \hat{L}_{m2} i_{qs} - (\omega_s L_{\sigma r} - \omega_r L_r) i_{qr} + R_{fe} i_{dfe} - \omega_r \hat{L}_{m2} i_{qfe} - \frac{3P^2\hat{L}_{m1}L_{\sigma r}\left(i_{qs}-i_{qfe}\right)e_\omega}{2J} \tag{51}$$

$$V^*_{qr} = k_4 e_{iqr} L_{\sigma r} + \frac{L_{\sigma r}}{(i_{ds}-i_{dfe})} \times \left\{-\frac{PT_t e_\omega}{\hat{L}^2_{m1}J^2}\left\{\left(i_{qs}-i_{qfe}\right)i_{dr} - \left(i_{ds}-i_{dfe}\right)i_{qr}\right\} - \frac{2{k_\omega}^2 e_\omega}{3P^2\hat{L}_{m1}} - \frac{k_\omega {e_\omega}^2}{J\hat{L}^2_{m1}}\left\{\left(i_{qs}-i_{qfe}\right)i_{dr} - \left(i_{ds}-i_{dfe}\right)i_{qr}\right\}\right\} + R_r i_{qr} - \omega_r \hat{L}_{m2} i_{ds} + (\omega_s L_{\sigma r} - \omega_r L_r) i_{dr} + R_{fe} i_{qfe} + \omega_r \hat{L}_{m2} i_{dfe} + \frac{3P^2 L_{\sigma r}\hat{L}_{m1}\left(i_{ds}-i_{dfe}\right)e_\omega}{2J}. \tag{52}$$

Hence, the derivative of the final Lyapunov function is expressed as (53) after replacing the terms V_{dr} and V_{qr} in (47) shown at the bottom of this page by utilizing (51) and (52) as

$$\dot{V}_{Fp} = -k_\omega e_\omega^2 - k_3 e_{idr}^2 - k_4 e_{iqr}^2. \tag{53}$$

$\dot{V}_{Fp}$ becomes a negative semidefinite function with positive feedback constants $k_\omega, k_3, k_4,$ and β. In the controller design, the nonlinearity effect of the machine appears due to the presence of the term $i_{dm} i_{qr}$ in the machine torque equation. The nonlinear terms are often ignored in linear controller design and system disturbances are avoided to eradicate complicacy in the cost of design accuracy. Linearization of the DFIG-WECS model cannot predict the nonlinear dynamics and nonlocal behavior far from the operating point for the overall system. Hence, the nonlinear controller in the proposed design helps to achieve fast dynamic behavior, which improves the transient response of the grid-connected DFIG, particularly under wind speed fluctuation and voltage disturbance.

$$
\begin{aligned}
\therefore \dot{V}_{Fp} &= \dot{V}_\omega + e_{idr}\dot{e}_{idr} + e_{iqr}\dot{e}_{iqr} + \frac{1}{\beta} e_{L2}\dot{e}_{L2} \\
&= \dot{V}_\omega + e_{idr}\left\{ \dot{i}_{dr}^* - \frac{1}{L_{\sigma r}}\left\{ V_{dr} - R_r i_{dr} - \omega_r L_m i_{qs} + \left(\omega_s L_{\sigma r} - \omega_r L_r\right) i_{qr} - R_{fe} i_{dfe} + \omega_r L_m i_{qfe} \right\} \right\} \\
&\quad + e_{iqr}\left\{ \dot{i}_{qr}^* - \frac{1}{L_{\sigma r}}\left\{ V_{qr} - R_r i_{qr} + \omega_r L_m i_{ds} - \left(\omega_s L_{\sigma r} - \omega_r L_r\right) i_{dr} - R_{fe} i_{qfe} - \omega_r L_m i_{dfe} \right\} \right\} + \frac{1}{\beta} e_{L2}\left(-\dot{\hat{L}}_{m2}\right) \\
&= -k_\omega e_\omega^2 + \frac{3P^2 \hat{L}_{m1}\left(i_{ds} - i_{dfe}\right) e_\omega e_{iqr}}{2J} - \frac{3P^2 \hat{L}_{m1}\left(i_{qs} - i_{qfe}\right) e_\omega e_{idr}}{2J} \\
&\quad + e_{idr}\left\{ -\frac{1}{L_{\sigma r}}\left\{ V_{dr} - R_r i_{dr} - \omega_r L_m i_{qs} + \left(\omega_s L_{\sigma r} - \omega_r L_r\right) i_{qr} - R_{fe} i_{dfe} + \omega_r L_m i_{qfe} \right\} \right\} \\
&\quad + e_{idr}\left[\frac{1}{\left(i_{ds} - i_{dfe}\right)} \left\{ -\frac{PT_t e_\omega}{\hat{L}_{m1}^2 J^2}\left\{ \left(i_{qs} - i_{qfe}\right) i_{dr} - \left(i_{ds} - i_{dfe}\right) i_{qr} \right\} - \frac{2k_\omega^2 e_\omega}{3P^2 \hat{L}_{m1}} - \frac{k_\omega e_\omega^2}{J\hat{L}_{m1}^2}\left\{ \left(i_{qs} - i_{qfe}\right) i_{dr} - \left(i_{ds} - i_{dfe}\right) i_{qr} \right\} \right\} \right. \\
&\quad \left. - \frac{1}{L_{\sigma r}}\left\{ V_{qr} - R_r i_{qr} + \omega_r L_m i_{ds} - \left(\omega_s L_{\sigma r} - \omega_r L_r\right) i_{dr} - R_{fe} i_{qfe} - \omega_r L_m i_{dfe} \right\} \right] \\
&\quad + \frac{1}{\beta} e_{L2}\left(-\dot{\hat{L}}_{m2}\right) = -k_\omega e_\omega^2 + \frac{3P^2 \hat{L}_{m1}\left(i_{ds} - i_{dfe}\right) e_\omega e_{iqr}}{2J} - \frac{3P^2 \hat{L}_{m1}\left(i_{qs} - i_{qfe}\right) e_\omega e_{idr}}{2J} + e_{idr} \\
&\quad \times \left\{ -\frac{1}{L_{\sigma r}}\left\{ V_{dr} - R_r i_{dr} - \omega_r \hat{L}_{m2} i_{qs} + \left(\omega_s L_{\sigma r} - \omega_r L_r\right) i_{qr} - R_{fe} i_{dfe} + \omega_r \hat{L}_{m2} i_{qfe} \right\} \right\} + e_{iqr} \\
&\quad \times \left[\frac{1}{\left(i_{ds} - i_{dfe}\right)} \left\{ -\frac{PT_t e_\omega}{\hat{L}_{m1}^2 J^2}\left\{ \left(i_{qs} - i_{qfe}\right) i_{dr} - \left(i_{ds} - i_{dfe}\right) i_{qr} \right\} - \frac{2k_\omega{}^2 e_\omega}{3P^2 \hat{L}_{m1}} - \frac{k_\omega e_\omega{}^2}{J\hat{L}_{m1}^2}\left\{ \left(i_{qs} - i_{qfe}\right) i_{dr} - \left(i_{ds} - i_{dfe}\right) i_{qr} \right\} \right\} \right. \\
&\quad \left. - \frac{1}{L_{\sigma r}}\left\{ V_{qr} - R_r i_{qr} + \omega_r \hat{L}_{m2} i_{ds} - \left(\omega_s L_{\sigma r} - \omega_r L_r\right) i_{dr} - R_{fe} i_{qfe} - \omega_r \hat{L}_{m2} i_{dfe} \right\} \right] \\
&\quad + \frac{1}{\beta} e_{L2}\left(-\dot{\hat{L}}_{m2}\right) + \frac{1}{L_{\sigma r}} e_{idr} e_{L2} \omega_r i_{qs} - \frac{1}{L_{\sigma r}} e_{idr} e_{L2} \omega_r i_{qfe} - \frac{1}{L_{\sigma r}} e_{iqr} e_{L2} \omega_r i_{ds} + \frac{1}{L_{\sigma r}} e_{iqr} e_{L2} \omega_r i_{dfe} \\
&= -k_\omega e_\omega^2 + e_{idr}\left[-\frac{1}{L_{\sigma r}}\left\{ V_{dr} - R_r i_{dr} - \omega_r \hat{L}_{m2} i_{qs} + \left(\omega_s L_{\sigma r} - \omega_r L_r\right) i_{qr} - R_{fe} i_{dfe} + \omega_r \hat{L}_{m2} i_{qfe} \right\} \right. \\
&\qquad \left. - \frac{3P^2 \hat{L}_{m1}\left(i_{qs} - i_{qfe}\right) e_\omega}{2J} \right] + e_{iqr}\left[\frac{1}{\left(i_{ds} - i_{dfe}\right)} \left\{ -\frac{PT_t e_\omega}{\hat{L}_{m1}^2 J^2}\left\{ \left(i_{qs} - i_{qfe}\right) i_{dr} - \left(i_{ds} - i_{dfe}\right) i_{qr} \right\} \right. \right. \\
&\qquad \left. \left. - \frac{2k_\omega{}^2 e_\omega}{3P^2 \hat{L}_{m1}} - \frac{k_\omega e_\omega{}^2}{J\hat{L}_{m1}^2}\left\{ \left(i_{qs} - i_{qfe}\right) i_{dr} - \left(i_{ds} - i_{dfe}\right) i_{qr} \right\} \right\} \right. \\
&\quad \left. - \frac{1}{L_{\sigma r}}\left\{ V_{qr} - R_r i_{qr} + \omega_r \hat{L}_{m2} i_{ds} - \left(\omega_s L_{\sigma r} - \omega_r L_r\right) i_{dr} - R_{fe} i_{qfe} - \omega_r \hat{L}_{m2} i_{dfe} \right\} + \frac{3P^2 \hat{L}_{m1}\left(i_{ds} - i_{dfe}\right) e_\omega}{2J} \right] \\
&\quad + e_{L2}\left\{ \frac{1}{L_{\sigma r}} e_{idr} \omega_r i_{qs} - \frac{1}{L_{\sigma r}} e_{idr} \omega_r i_{qfe} - \frac{1}{L_{\sigma r}} e_{iqr} \omega_r i_{ds} + \frac{1}{L_{\sigma r}} e_{iqr} \omega_r i_{dfe} - \frac{\dot{\hat{L}}_{m2}}{\beta} \right\}
\end{aligned}
\tag{47}
$$

IV. Adaptation of Machine Parameters

For control purpose, usually the nominal values of the machine parameter are utilized. For a grid-connected DFIG, the stator and rotor winding resistance and leakage reactance are considered to remain unchanged as the supply frequency is constant and the temperature variation is insignificant. However, the magnetizing inductance value may alter at a different level of magnetization. At variable wind speed, the RSC regulates the speed and flux of the machine and the level of magnetization too. Thus, it necessitates the adaptation of magnetizing inductance during operation [20]. The magnetizing inductance is updated online to cope with the variations. The update rule for the inductance is defined in (54), which is obtained from (50)

$$\dot{\hat{L}}_{m2} = \beta \left(\frac{1}{L_{\sigma r}} e_{idr}\omega_r i_{qs} - \frac{1}{L_{\sigma r}} e_{idr}\omega_r i_{qfe} - \frac{1}{L_{\sigma r}} e_{iqr}\omega_r i_{ds} + \frac{1}{L_{\sigma r}} e_{iqr}\omega_r i_{dfe} \right). \tag{54}$$

Since the error variable e_{L2} is absent in (53), only the boundedness of the state variables is proven from the abovementioned derivation. The system is assumed to be autonomous. So, we can use LaSalle's theorem to check whether the equilibrium point is asymptotically stable.

Let us assume, $\dot{V}_{Fp} = 0$.

Utilizing (53), we get, $e_\omega = 0, e_{idr} = 0, e_{iqr} = 0$.

$$\therefore \dot{e}_{idr} = 0, \dot{e}_{iqr} = 0.$$

Applying the control voltages from (51) and (52) into the state error equations, we obtain

$$\begin{aligned} \dot{e}_{idr} &= -k_3 e_{idr} + e_{L2}\left(i_{qs}\omega_r^* - i_{qs}e_\omega - \omega_r^* i_{qfe} + e_\omega i_{qfe}\right) \\ &= -k_3 e_{idr} + e_{L2}\left(i_{qs}\omega_r^* - i_{qs}e_\omega - \omega_r^* i_{qfe} + e_\omega i_{qfe}\right) \end{aligned} \tag{55}$$

$$\begin{aligned} \dot{e}_{idr} &= -k_4 e_{iqr} + e_{L2}\left(i_{ds}\omega_r^* - i_{ds}e_\omega - \omega_r^* i_{dfe} + e_\omega i_{dfe}\right) \\ &= -k_4 e_{iqr} + e_{L2}\left(i_{ds}\omega_r^* - i_{ds}e_\omega - \omega_r^* i_{dfe} + e_\omega i_{dfe}\right). \end{aligned} \tag{56}$$

Applying $e_\omega = 0, e_{idr} = 0, e_{iqr} = 0$ in (55) and (56), it is found that $e_{L2} = 0$, under the conditions of $i_{ds} \neq i_{dfe}$ and $i_{qs} \neq i_{qfe}$. On the contrary, by plugging the error variable values in (44), no decision can be made about the convergence of the error variable e_{L1}. Therefore, it can be concluded that the equilibrium point $(e_\omega, e_{idr}, e_{iqr}, e_{L2}) = 0$ is globally asymptotically stable. Also, the estimated magnetization inductance $\hat{L}_{m2}$ will converge to the rated value. Hence, by utilizing the adaptive backstepping based nonlinear control, the stability of the rotor converter control loop is achieved. The equation for the estimation of the magnetization inductance is also obtained from it.

V. Loss Minimization Algorithm

The loss minimization algorithm for the proposed model of DFIG is evaluated based on stator voltage oriented control scheme, i.e., $v_{qs} = 0$. At steady state, from Fig. 2(a) and (b), it can be derived that

$$i_{dfe} = \frac{\omega_s L_m}{R_{fe}}\left(i_{dm} - i_{qm}\right) \tag{57}$$

$$i_{qfe} = \frac{\omega_s L_m}{R_{fe}}\left(i_{dm} + i_{qm}\right). \tag{58}$$

By utilizing the *d-q* axis equivalent circuit for the stator voltage oriented control scheme, the following equations are obtained:

$$i_{ds} = \frac{V_s - \omega_s L_m i_{dm}}{R_s} \tag{59}$$

$$i_{qs} = -\frac{\omega_s L_m i_{qm}}{R_s} \tag{60}$$

$$i_{qr} = \left(1 + \frac{2s\omega_s L_m}{R_{fe}}\right) i_{qm} + \frac{s\omega_s L_m i_{dm}}{R_s} \tag{61}$$

$$i_{dm} = i_{qm} - \frac{R_{fe} i_{qfe}}{\omega_s L_m}. \tag{62}$$

By utilizing (9)–(12) and (57)–(62) and performing the differentiation, the following equations can be obtained:

$$\frac{di_{ds}}{di_{dr}} = -\frac{\omega_s L_m}{R_s}\frac{di_{dm}}{di_{dr}} \tag{63}$$

$$\frac{di_{qs}}{di_{dr}} = -\frac{\omega_s L_m}{R_s}\frac{di_{qm}}{di_{dr}} \tag{64}$$

$$\frac{di_{qr}}{di_{dr}} = \left(1 + \frac{2s\omega_s L_m}{R_{fe}}\right)\frac{di_{qm}}{di_{dr}} + \frac{s\omega_s L_m}{R_{fe}}\frac{di_{dm}}{di_{dr}} \tag{65}$$

$$\frac{di_{dfe}}{di_{dr}} = 1 + \left(\frac{\omega_s L_m}{R_s} - 1\right)\frac{di_{dm}}{di_{dr}} \tag{66}$$

$$\frac{di_{dfe}}{di_{dr}} = 1 + \left(\frac{\omega_s L_m}{R_s} - 1\right)\frac{di_{dm}}{di_{dr}} \tag{67}$$

$$\frac{di_{qfe}}{di_{dr}} = \frac{s\omega_s L_m}{R_{fe}}\frac{di_{dm}}{di_{dr}} + \left(\frac{2s\omega_s L_m}{R_{fe}} - \frac{\omega_s L_m}{R_s}\right)\frac{di_{qm}}{di_{dr}} \tag{68}$$

$$\frac{di_{qm}}{di_{dr}} = \left(\frac{2R_s}{R_{fe} - R_s}\right)\frac{di_{dm}}{di_{dr}}. \tag{69}$$

By assuming $R_{fe} \gg \omega_s L_m$, the following equation is derived:

$$\frac{di_{dm}}{di_{dr}} = \frac{R_s}{R_s + \omega_s L_m}. \tag{70}$$

The overall resistive power loss in DFIG is defined as

$$P_{\text{loss}} = R_s\left(i_{ds}^2 + i_{qs}^2\right) + R_r\left(i_{dr}^2 + i_{qr}^2\right) + R_{fe}(i_{dfe}^2 + i_{qfe}^2). \tag{71}$$

The loss will be minimized when $\frac{dP_{\text{loss}}}{di_{dr}} = 0$.Thus,

$$R_s\left(i_{ds}\frac{di_{ds}}{di_{dr}} + i_{qs}\frac{di_{qs}}{di_{dr}}\right) + R_r\left(i_{dr} + i_{qr}\frac{di_{qr}}{di_{dr}}\right) + R_{fe}\left(i_{dfe}\frac{di_{dfe}}{di_{dr}} + i_{qfe}\frac{di_{qfe}}{di_{dr}}\right) = 0. \tag{72}$$

TABLE II
SIMULATION PARAMETERS FOR PI AND NONLINEAR CONTROLLERS

PI Controller Parameters	Simulation data	Nonlinear Controller Parameters	Simulation data
$K_{p,vbus}$, $K_{i,vbus}$	-10^4,-3×10^5	k_1,k_2	30, 50
$K_{p,idr}$, $K_{i,idr}$	1.3×10^4, 350	k_3,k_4	80, 100
$K_{p,iqr}$, $K_{i,iqr}$	4.5×10^2,55	k_ω,k_{ebus}	50,30
$K_{p,ids}$,$K_{i,ids}$	0.03,0.3	β	1.4×10^{-12}
$K_{p,iqs}$,$K_{i,iqs}$	0.289,3.2		

By replacing the machine parameter terms with constants

$$\frac{di_{dm}}{di_{dr}} = \frac{R_s}{R_s+\omega_s L_m} = A,\ \frac{s\omega_s L_m}{R_{fe}} = B,\ \frac{\omega_s L_m}{R_s} = C,\ \frac{2R_s}{R_{fe}-R_s} = D.$$

Equation (72) can be simplified as

$$R_s(-CAi_{ds} - CDAi_{qs}) + R_r\left(i_{dr}+i_{qr}\left((1+2B)DA+BA\right)\right) + R_{fe}\left(\left(i_{ds}+i_{dr}-\frac{R_s i_{dr}-V_s}{R_s+\omega_s L_m}\right)\{(C-1)A+1\} + \left\{\left(\frac{C}{1+C}\right)i_{qs}+i_{qr}\right\}\{BA+2B-C\}DA\right) = 0. \tag{73}$$

Finally, the condition for loss reduction model obtains the following form:

$$i_{dr}^* = \frac{R_s CA\left(i_{ds}+Di_{qs}\right) - R_r\left(i_{qr}\left((1+2B)DA+BA\right)\right) - R_{fe}\left(\begin{array}{l}\left(i_{ds}+\frac{V_s}{R_s+\omega_s L_m}\right)\{(C-1)A+1\} \\ +\left\{\left(\frac{C}{1+C}\right)i_{qs}+i_{qr}\right\}\{BA+2B-C\}DA\end{array}\right)}{R_r + R_{fe}(C-1)A+1)(1-A)}. \tag{74}$$

The control signal i_{dr}^* is dependent on d-q axis stator current, q-axis rotor current component, supply voltage and frequency, which can be obtained from current, voltage, and speed sensors. The machine ratings and adaptation rules provide the required resistance, inductance, and constant parameters. The inclusion of iron loss component in the proposed controller ensures precision in the loss reduction model.

VI. SIMULATION RESULTS

The performance of the proposed nonlinear controller integrated with machine loss reduction for DFIG-based WECS is investigated in simulation at different operating conditions with MATLAB/Simulink model. The nonlinear controllers are designed to force the error function of the state variables to the null point and thus, stabilize the machine about the desired equilibrium state. The simulation results of the proposed controller are compared with the conventional PI controlled converter and sliding mode converter control operation in DFIG-WECS. The simulation parameters of the designed controllers are presented in Table II.

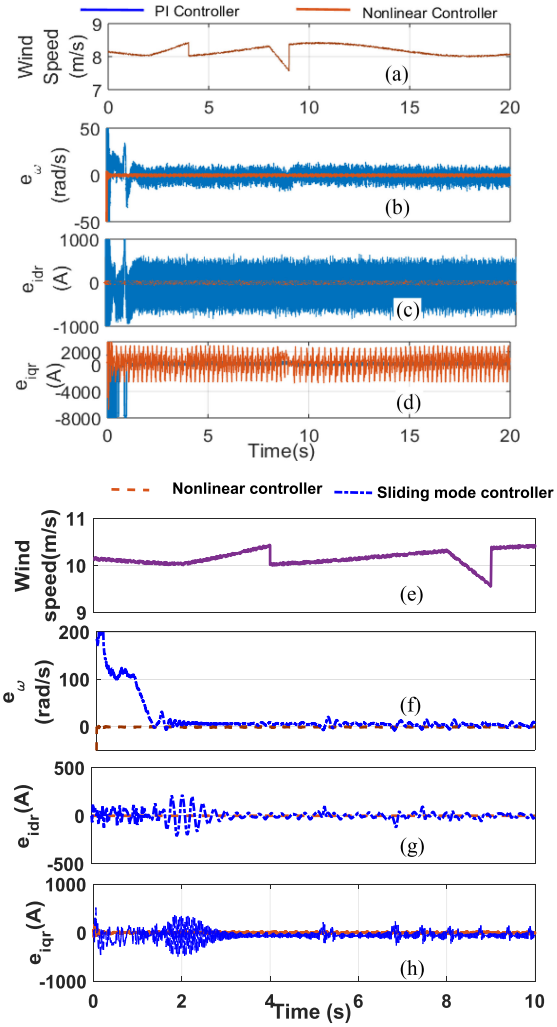

Fig. 3. Comparison of simulation performances between controllers for RSC control of DFIG under variable wind speed. (a)–(d) Comparison between PI and nonlinear controller: (a) Variation in wind speed. (b) Rotor speed error (rad/s). (c) d-axis rotor current error. (d) q-axis rotor current error. (e)–(h) Comparison between the SMC and the nonlinear controllers. (e) Variation in wind speed. (f) Rotor speed error. (g) d-axis rotor current error. (h) q-axis rotor current error.

A. RSC Control Performance

The RSC control is used to track the reference rotor speed generated by the MPPT controller. The RSC control block produces control voltages (V_{dr}^* and V_{qr}^*) according to (51) and (52). The performance of the proposed nonlinear controller for RSC control is compared with the traditional PI controller and displayed in Fig. 3(a)–(d). It is evident from Fig. 3(b) that the rotor speed error exhibit less fluctuation for the proposed nonlinear controller as compared to the PI controller. For d-q axis rotor current errors, it is found that for d-axis rotor current, the nonlinear controllers demonstrate better performance, whereas, the current errors from the PI controller are less than its counterpart for q-axis rotor current. The performance of the nonlinear controller is also compared with the sliding mode controller as shown in Fig. 3(e)–(h). The wind speed variation is shown in Fig. 3(e). The red and blue dotted lines specify the

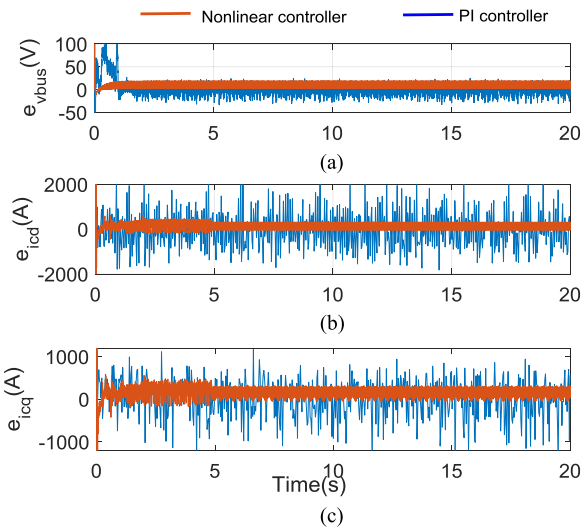

Fig. 4. Comparison of simulation performances between PI controller and proposed nonlinear controller for GSC control of DFIG under variable wind speed. (a) DC-link voltage error. (b) d-axis grid converter current error. (c) q-axis grid converter current error.

error variables for the nonlinear control and the sliding mode control (SMC) operation, respectively. The detailed model of SMC for the RSC control of DFIG-WECS can be found in [22]. In practical applications, sliding mode controllers are affected by the undesirable oscillatory phenomenon, which is known as chattering. It is evident that the rotor speed error [see Fig. 3(f)] and the d-axis and q-axis rotor current errors [see Fig. 3(g) and (h)] from the nonlinear controller are much smaller than those of the sliding mode controller. The fluctuations from the SMC are relatively high due to its chattering effect. The error minimization feature proves the distinctiveness of the proposed nonlinear controller. By following the reference speed produced by the MPPT controller, the proposed controller ensures maximum power extraction from the wind turbine.

B. GSC Control Performance

The target of the GSC control is to regulate the dc-link voltage. The controller forces the error function (e_{vbus}, e_{icd} and e_{icq}) to converge to zero. Fig. 4 displays the comparative analysis between the nonlinear controller and PI controller based GSC control operation. The dc-link voltage error is asymptotically diminished as shown in Fig. 4(a). The converter current error functions depict better asymptotic convergence for the proposed controller compared to the PI counterpart [see Fig. 4(b) and (c)]. To design the RSC and GSC control, the constants k_1, k_2, k_3, k_4, k_ω, and β are deliberately chosen as given in Table II to ensure that the desired error functions are minimized.

Fig. 5 exhibits the comparative analysis between the virtual control inputs for the proposed nonlinear control and conventional PI control of the RSC and GSC. Fig. 5(a) and (b) show the d-q axis rotor control voltages for nonlinear and PI controlled RSC, respectively. The variation of q-axis rotor control voltage (V_{qr}^*) is affected by the change of wind speed and corresponding

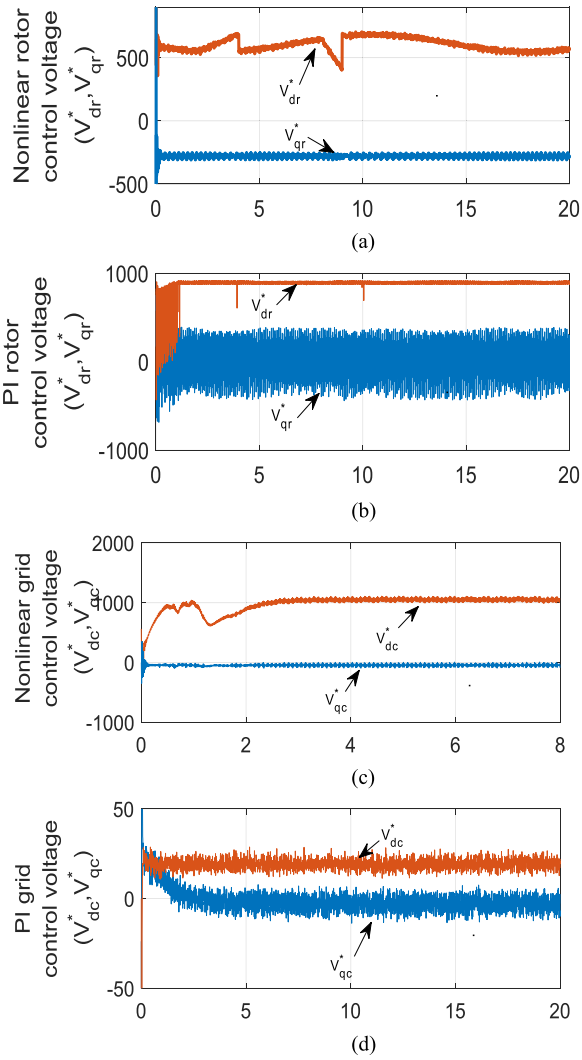

Fig. 5. Control input voltage comparison between the proposed nonlinear controller and PI controller for GSC and RSC control of DFIG under variable wind speed. (a) Nonlinear rotor control voltages. (b) PI controlled rotor control voltages for RSC. (c) Nonlinear grid converter control voltages. (d) Control voltages for grid side converter under PI control.

generator torque whereas the reference d-axis rotor current enforce the alteration of d-axis rotor control voltage (V_{qr}^*). Fig. 5(c) and (d) depict the d-q axis virtual control voltages for the GSC for proposed nonlinear and PI controller, respectively.

The nonlinear controlled system differs from the PI controlled converters in terms of three reference parameters, e.g., $V_{\text{bus,ref}}$, i_{qr}^*, and i_{dc}^*. In PI controlled system, the dc-link reference voltage is stabilized at 1150 V, whereas it is determined by (30) in nonlinear control. Similarly, the q-axis rotor reference current can be obtained according to $i_{qr}^* = \frac{T_{em}}{-1.5P\frac{L_m}{L_s}|\psi_s|}$ for PI control while (45) provides i_{qr}^* for nonlinear control.

Likewise, the d-axis grid converter current (i_{dc}^*) is different for respective controllers. Moreover, adaptive backstepping based nonlinear controller has high gain values. Due to the effect of all these factors, the control input voltages of PI controlled DFIG-WECS differ from the adaptive backstepping based nonlinear

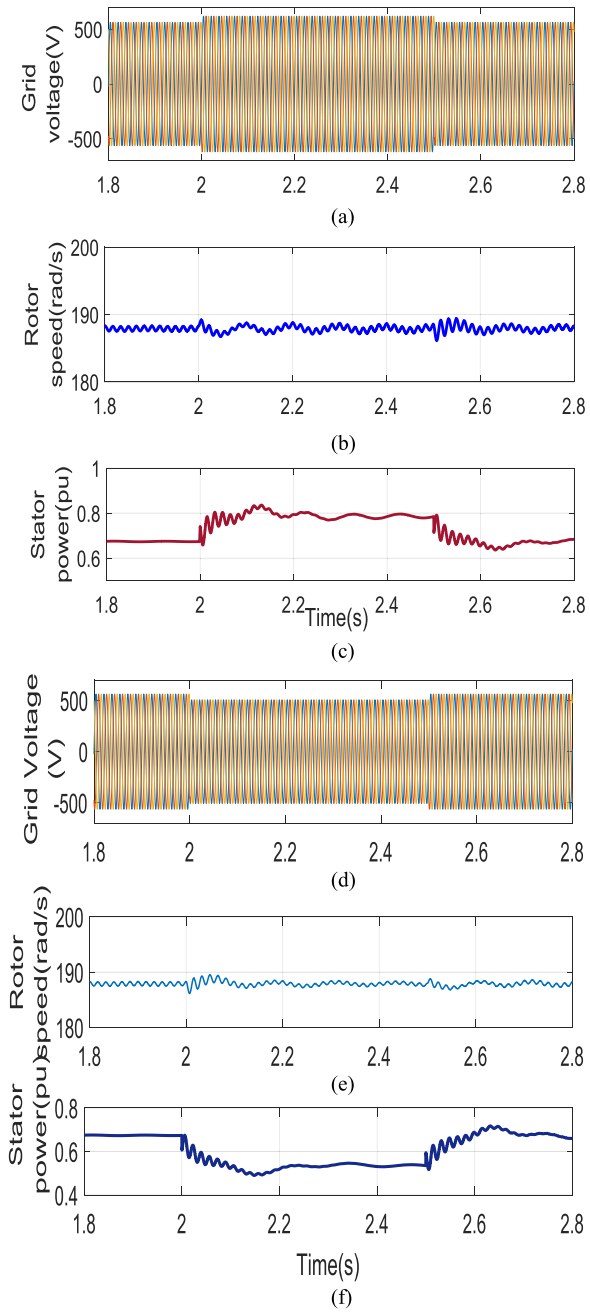

Fig. 6. Generator output performance for a momentary change in grid voltage for wind speed of 10 m/s. (a) 10% increase in grid voltage between t = 2–2.5 s. (b) Corresponding change in rotor speed. (c) Stator power output in p.u. (d) 10% dip in grid voltage between t = 2–2.5 s. (e) Corresponding change in rotor speed. (f) Stator power output in p.u.

controlled module for the grid-side and rotor-side converters. One of the typical sources of instability, which might unsettle a grid-connected system, is grid voltage fluctuation. Distortion at grid side can be originated from the addition of reactive power compensation equipment, nonlinear load condition or by sudden phase voltage failure. A nonlinear controlled RSC is a suitable option to handle the grid voltage fluctuation, which prevents the machine from running into the failure zone. Fig. 6 illustrates the ability of the proposed nonlinear system to settle down if

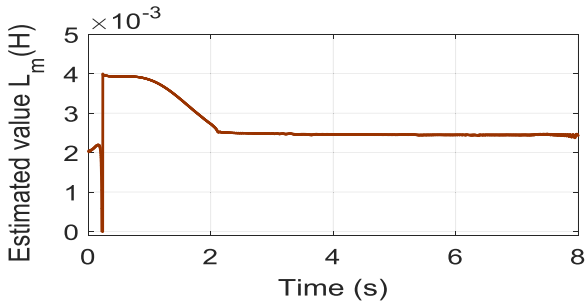

Fig. 7. Estimated value of the magnetizing inductance.

the DFIG undergoes under any abnormality at grid voltage. The system is simulated for 10% increase and decrease in grid voltage for 0.5 s [see Fig. 6(a) and (d)]. It is observed that the DFIG rotor speed [see Fig. 6(b)] and stator power [see Fig. 6(c)] has been recovered quickly after transitory fluctuation caused by the sudden rise of grid voltage. The variation in rotor speed is also negligible due to the symmetric voltage dip at the grid end [see Fig. 6(e)] and stator power [see Fig. 6(f)] decreases according to the variation of the grid voltage. The simulations for abnormal grid-voltage conditions are performed in rated wind speed with reference rotor speed selected at the synchronous value. The parameter update law in (54) provides the estimated value of magnetizing inductance. Fig. 7 demonstrates the estimated output at the rated condition. The estimated magnetizing inductance stays very close (L_m= 2.5 mH) to the rated value at steady state.

Finally, the loss minimization block is activated to reduce the total power loss of the machine. Fig. 8 illustrates the block diagram and performance of the loss reduction scheme. Fig. 8(a) demonstrates the block diagram for the calculation of d-axis rotor reference current that executes the machine loss minimization scheme. The wind speed is varied to observe the performance of the loss reduction block at a variable rotor speed. Fig. 8(b) illustrates the efficacy of the loss minimization scheme. The machine loss is compared by activating and deactivating the loss minimization block for different rotor speeds of DFIG. It is observed that the power loss reduces significantly for the entire range of speed variation while the loss minimization module is activated. Thus, the proposed scheme provides power savings and economic operation of the DFIG-driven WECS. From Fig. 8(c), it is perceived that average machine loss is reduced by 1.7% from its initial value after the loss minimization algorithm is activated at rated wind speed. The changes in reference rotor currents are shown in Fig. 8(d) and (e) to illustrate the effect of the activation of the loss reduction block. The sensitivity of the loss reduction model has been tested for the variation of rotor resistance (R_r). The core loss in a generator is almost constant with fixed stator flux, whereas the copper losses may vary under variable load or grid demand condition. The variation in rotor speed and temperature can affect the rotor resistance, and any change in rotor resistance will reflect proportionally to machine power loss. Hence, machine loss minimization models are sensitive to the variation in rotor resistance.

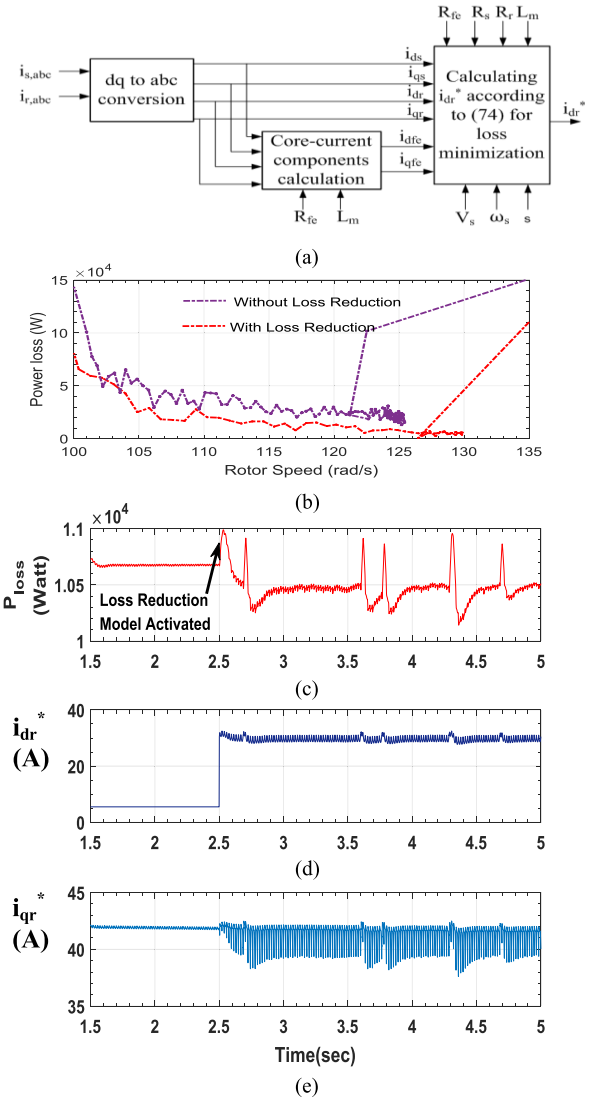

Fig. 8. Effect of machine loss minimization scheme. (a) Block diagram of the loss reduction scheme. (b) Power loss comparison with and without activation of the loss reduction model for variable rotor speed. (c) Overall machine loss with loss reduction model is activated at t = 2.5 s. (d) Corresponding change in reference *d*-axis rotor current. (e) Reference *q*-axis rotor current.

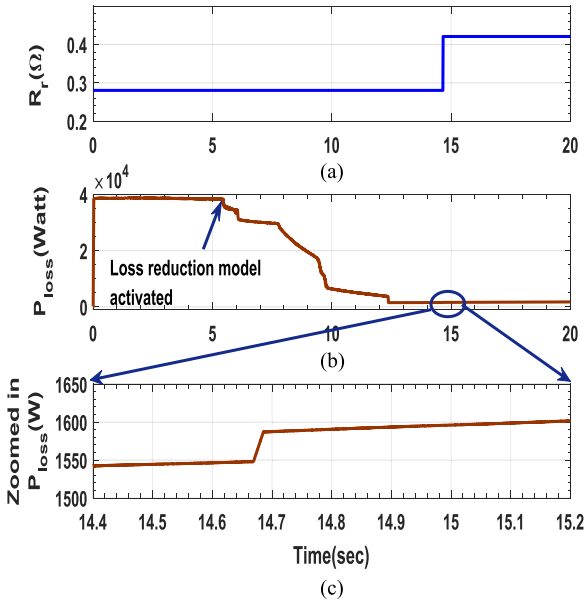

Fig. 9. Parameter sensitivity analysis for proposed loss minimization scheme. (a) Increment of rotor resistance by 50% during simulation at t = 14.65 s. (b) Overall machine loss in watt when loss reduction model is activated at t = 5.5 s. (c) Zoom-in view for power loss in watt at the instant of the change in rotor resistance.

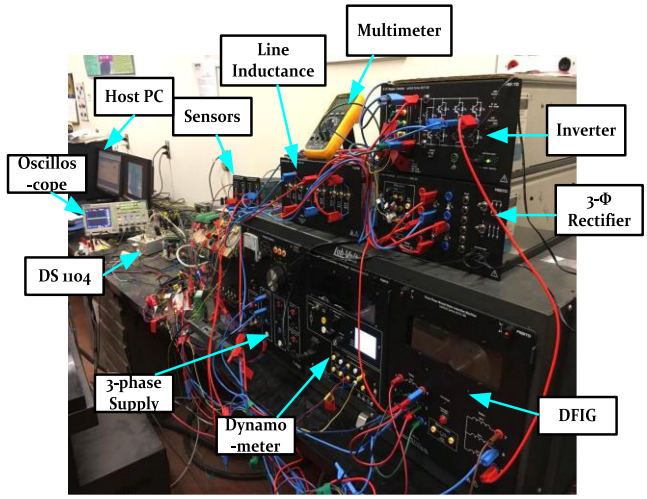

Fig. 10. Experimental setup for the proposed DFIG-based WECS.

In this article, the rotor winding resistance sensitivity on the loss reduction model is tested in simulation. Fig. 9 demonstrates the effectiveness of loss reduction model in simulation with the variation of the rotor winding resistance. It is observed from Fig. 9(b) that when the loss reduction model is activated at t = 5 s, the power loss reduces significantly and settles after 12.5 s. The rotor resistance is increased by 50% of its rated value at t = 14.65 s [see Fig. 9(a)], but the increase in corresponding power loss is only 1.6%, which is very insignificant. To clarify the result, the zoom-in view of Fig. 9(b) is plotted in Fig. 9(c).

VII. Real-Time Implementation and Results

A prototype for the proposed nonlinear controller based DFIG-WECS has been assembled to observe the performance in real time. The experimental setup for the prototype 480 VA LabVolt series DFIG-based WECS is shown in Fig. 10, where the wound rotor induction machine is utilized as the DFIG. The dynamometer module comprises the wind-turbine emulator facilitating the variation of turbine torque with the change of equivalent wind speed. The GSC control is avoided to reduce the complexity of the system. A three-phase full-wave diode rectifier is used as the GSC, which provides fixed dc-link voltage. During the experiment, the wind speed is varied from the input control panel to observe the variation of control variables of the proposed nonlinear controller model. The PWM is generated by the DSP board DS1104 to control RSC.

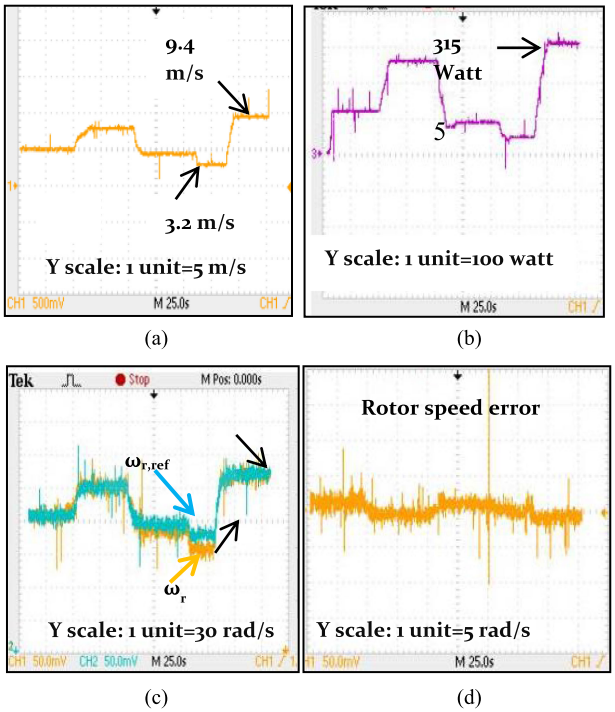

Fig. 11. Experimental performance of the proposed nonlinear controller based DFIG-WECS. (a) Variation in wind speed generated by the turbine emulator. (b) Corresponding power produced by the DFIG. (c) Reference and actual rotor speed. (d) Rotor speed error.

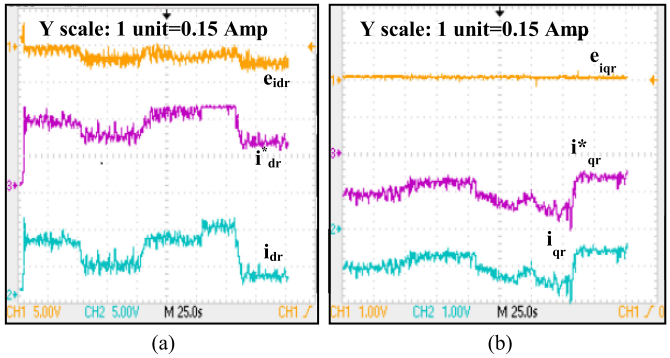

Fig. 12. Experimental performance of the proposed nonlinear controller based RSC of DFIG. (a) Reference and actual d-axis rotor currents and corresponding error. (b) Reference and actual q-axis rotor currents and current error.

Fig. 11 illustrates the variation of wind speed and the power generated by the machine [see Fig. 11(a) and (b)]. The wind speed is emulated to vary in between 3.2 and 9.4 m/s. The HCS algorithm based MPPT controller provides the rotor reference speed for the controller, and the DFIG reacts accordingly to follow the speed. Thus, the controller ensures the maximum power extraction by minimizing the rotor speed error under variable wind speed as demonstrated in Fig. 11(c) and (d). The graphs suggest that the proposed nonlinear controller is capable of minimizing the speed error under variable wind speed. The performance of the nonlinear controller depends on the elimination of d-q axis current error functions. Fig. 12 demonstrates the

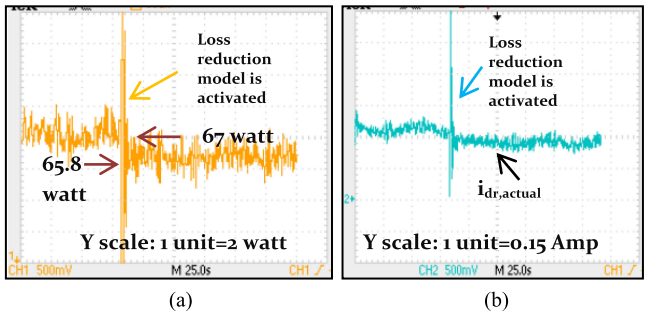

Fig. 13. Experimental performance of the machine loss reduction model. (a) Total power loss before and after the activation of loss reduction algorithm. (b) Corresponding change in d-axis rotor current of DFIG.

performance of the nonlinear controller designed for the RSC. The d- and q-axis rotor currents follow the reference values competently while the wind speed is varied according to the wind profile displayed in Fig. 10(a). The d-axis rotor current error fluctuates around zero axis [see Fig. 12(a)], whereas the q-axis rotor current is precisely nullified by the controller action [see Fig. 12(b)].

Fig. 13 demonstrates the performance of the proposed machine loss reduction algorithm developed for the doubly-fed machine. After the activation of the loss reduction algorithm, the average estimated copper power loss of the DFIG is reduced by 1.8% from its initial value for input torque of 0.9 N·m [see Fig. 13(a)]. The loss reduction is significant for large scale industrial wind turbine generator. The variation in d-axis rotor current is caused by the change of the corresponding reference current to reduce the machine losses [see Fig. 13(b)]. The successful implementation of loss reduction block ensures enhanced efficiency of the overall DFIG-WECS.

VIII. Conclusion

A novel nonlinear control strategy incorporated with loss minimization and parameter uncertainties for DFIG-based WECS has been proposed in this article to ensure stability and enhanced dynamic performance of the wind energy system. The state-space model of a DFIG is developed incorporating iron loss component to minimize the losses. The nonlinear control scheme utilizes the adaptive backstepping algorithm to generate the control voltages separately for both the grid side and RSCs. The proposed controller guarantees the convergence of error functions of the state variables to the null point and affirms maximum power extraction through reference rotor speed tracking. Considering the uncertainty of magnetizing inductance under dynamic operating condition, a parameter estimation model is formulated. Furthermore, a loss minimization algorithm incorporating iron loss has been devised to enhance the efficiency of DFIG by reducing the total power loss. The performance of the proposed DFIG-based WECS has been tested and compared with the benchmark tuned PI controller and SMC controller under different operating conditions such as variable wind speed, grid voltage disturbance, and parameter uncertainties. The simulation and experiment results demonstrate that the proposed

control scheme exhibits better grip over the rotor side and GSC control compared to the conventional PI controller and SMC by diminishing the error function. Besides the proficiency of the proposed loss reduction model is also verified by the experimental results for the prototype model of the DFIG-WECS.

REFERENCES

[1] T. Ackermann, *Wind Power in Power Systems*, 1st ed. New York, NY, USA: Wiley, 2005, pp. 68–69.

[2] R. Pena, J. C. Clare, and G. M. Asher, "Doubly fed induction generator using back-to-back PWM converters and its application to variable speed wind-energy generation," *IEEE Proc. Elect. Power Appl.*, vol. 143, no. 3, pp. 231–241, May 1996.

[3] A. Yazdani and R. Iravani, *Voltage-Sourced Converters in Power Systems: Modeling, Control, and Applications*, Hoboken, NJ, USA: Wiley, 2010.

[4] H. Nian, P. Cheng, and Z. Q. Zhu, "Coordinated direct power control of DFIG system without phase-locked loop under unbalanced grid voltage conditions," *IEEE Trans. Power Electron.*, vol. 31, no. 4, pp. 2905–2917, Apr. 2016.

[5] S. Z. Chen, N. C. Cheung, K. C. Wong, and J. Wu, "Integral sliding-mode direct torque control of doubly-fed induction generators under unbalanced grid voltage," *IEEE Trans. Energy Convers.*, vol. 25, no. 2, pp. 356–368, Jun. 2010.

[6] M. K. Bourdoulis and A. T. Alexandridis, "Direct power control of DFIG wind systems based on nonlinear modeling and analysis," *IEEE J. Emerg. Sel. Topics Power Electron.*, vol. 2, no. 4, pp. 764–775, Dec. 2014.

[7] J. Hu, J. Zhu, and D.G. Dorrel, "A comparative study of direct power control of AC/DC converters for renewable energy generation," in *Proc. 37th Annu. Conf. IEEE Ind. Electron. Soc.*, Melbourne, VIC, Australia, 2011, pp. 3578–3583.

[8] M. A. Rahman, D. M. Vilathgamuwa, M. N. Uddin, and K. Tseng, "Nonlinear control of interior permanent-magnet synchronous motor," *IEEE Trans. Ind. Appl.*, vol. 39, no. 2, pp. 408–416, Mar./Apr. 2003.

[9] W. Qiao, L Qu, and R. G. Harley, "Control of IPM synchronous generator for maximum wind power generation considering magnetic saturation," *IEEE Trans. Ind. Appl.*, vol. 45, no. 3, pp. 1095–1105, May 2009.

[10] P. Xiong and D. Sun, "Backstepping-based DPC strategy of a wind turbine-driven DFIG under normal and harmonic grid voltage," *IEEE Trans. Power Electron.*, vol. 31, no. 6, pp. 4216–4225, Jun. 2016.

[11] N. Khemiri, A. Khedher, and M. F. Mimouni, "A backstepping control strategy applied to the connected hybrid renewable energy system operated in MPPT," in *Proc. 8th Int. Conf. Exhib. Ecological Vehicles Renewable Energies*, Monte Carlo, Monaco, 2013, pp. 1–10.

[12] M. E. Azzaoui, H. Mahmoudi, and C. Ed-dahmani, "Backstepping control of a doubly fed induction generator integrated to wind power system," in *Proc. 2nd Int. Conf. Elect. Inf. Technol.*, Tangiers, Morocco, 2016.

[13] J. Koupeny, M. Siebrecht, S. Luecke, and A. Mertens, "Observer-based online parameter estimation of doubly fed induction generators based on the gradient descent method," in *Proc. Int. ETG Congr.*, Bonn, 2015, pp. 1–8.

[14] B. Bossoufi, M. Karim, A. Lagrioui, M. Taoussi, and A. Derouich, "Observer backstepping control of DFIG-Generators for wind turbines variable-speed: FPGA-based implementation," *Renewable Energy*, vol. 81, pp. 903–917, 2015.

[15] X. Wang, D. Sun, and Z. Q. Zhu, "Resonant-based backstepping direct power control strategy for DFIG under both balanced and unbalanced grid conditions," *IEEE Trans. Ind. Appl.*, vol. 53, no. 5, pp. 4821–30, Sep. 2017.

[16] Y.T. Weng and Y.Y. Hsu, "Sliding mode regulator for maximum power tracking and copper loss minimization of a doubly fed induction generator," *IET Renewable Power Gener.*, vol. 9, pp. 297–305, 2015.

[17] B. Chen, T. Lu, Y. Hsu, W. Chen, and Z. Lee, "An analytical approach to maximum power tracking and loss minimization of a doubly fed induction generator considering core loss," *IEEE Trans. Energy Convers.*, vol. 27, no. 2, pp. 449–456, Jun. 2012.

[18] I. K. Amin and M. N. Uddin, "Nonlinear control operation of DFIG based WECS with stability analysis," in *Proc. IEEE Ind. Appl. Soc. Annu. Meeting*, Cincinnati, OH, USA, pp. 1–8, Oct. 2017.

[19] R. H. Nelson, T. A. Lipo, and P.C. Krause, "Stability analysis of a symmetrical induction machine," *IEEE Trans. Power App. Syst.*, vol. PAS-88, no. 11, pp. 1710–1717, Nov. 1969.

[20] G. Abad, J. López, M. Rodríguez, L. Marroyo, and G. Iwanski, *Doubly Fed Induction Machine, Modeling and Control for Wind Energy Generation*. New York, NY, USA: Wiley, 2011.

[21] P. C. Krause and C. H. Thomas, "Simulation of symmetrical induction machinery," *IEEE Trans. Power App. Syst.*, vol. 84, no. 11, pp. 1038–1053, Nov. 1965.

[22] M. I. Martinez, A. Susperregui, G. Tapia, and H. Camblong, "Sliding-mode control for a DFIG-based wind turbine under unbalanced voltage," in *Proc. 18th World Congr.-Int. Federation Autom. Control*, Milano, Italy, pp. 538–543, Sep. 2011.

Ifte Khairul Amin (S'16–M'19) received the B.Sc. and M.Sc. degrees in electrical and electronic engineering from the Bangladesh University of Engineering and Technology, Dhaka, Bangladesh, in 2009 and 2014, respectively, and the Ph.D. degree in electrical engineering from Lakehead University, Thunder Bay, ON, Canada, in 2019.

He is currently an Assistant Professor with the Department of Electrical and Electronic Engineering, Shahjalal University of Science and Technology, Sylhet, Bangladesh. He has authored/co-authored more than 15 papers in international journals and conferences. His research interests include power electronic converter, wind energy conversion system, and intelligent control.

Mohammad Nasir Uddin (S'98–M'00–SM'04) received the B.Sc. and M.Sc. degrees in electrical and electronic engineering from Bangladesh University of Engineering and Technology, Dhaka, Bangladesh, in 1993 and 1996, respectively, and the Ph.D. degree in electrical engineering from the Memorial University of Newfoundland, St. John's, NL, Canada, in 2000.

He is currently a Professor with the Department of Electrical Engineering, Lakehead University, Barrie campus, ON, Canada. He is also a Visiting Professor (part-time, 2018–2021) with the Institute of Power Engineering, Universiti of Tenaga Nasional, Putrajaya, Malaysia. He has authored/coauthored more than 225 papers in international journals (49 in IEEE Transactions/Journals) and conferences. His research interests include power electronics, renewable energy, motor drives, and intelligent controller applications.

Dr. Uddin is currently an Associate Editor with the IEEE TRANSACTIONS ON INDUSTRY APPLICATIONS. He was one of the Technical Program Committee Chairs for IEEE Energy Conversion Congress and Expo (ECCE) 2015 at Montreal, Canada. He was an Executive Board Member of IEEE Industry Applications Society (IAS) and Chair of IEEE-IAS-Manufacturing Systems Development and Applications Department (2016–2017). He was the Technical Committee Chair for the IEEE-IAS [Industrial Automation and Control Committee (IACC)] Annual Meetings in 2011 and 2012. He was a Transactions Papers Review Chair (2009–2010 and 2013–2014) of the IEEE TRANSACTIONS ON INDUSTRY APPLICATIONS (IACC). Earlier, he was with IEEE IAS IACC for nine years in different capacities. Due to his outstanding contributions to IEEE-IAS, IACC recognized him with IEEE IAS Service Award 2015. He was the recipient of LU Distinguished Researcher Award 2010. He was also the recipient of four Prize Paper Awards from IEEE IAS IACC. He is a Registered Professional Engineer in the province of Ontario, Canada.